

Boundary Layers of Accretion Disks: Wave-Driven Transport and Disk Evolution

Matthew S. B. Coleman,^{1,2*} Roman R. Rafikov,^{1,3†} Alexander A. Philippov⁴

¹*Institute for Advanced Study, Einstein Drive, Princeton, NJ 08540, USA*

²*Department of Astrophysical Sciences, 4 Ivy Lane, Princeton University, Princeton, NJ 08540, USA*

³*Centre for Mathematical Sciences, Department of Applied Mathematics and Theoretical Physics, University of Cambridge, Wilberforce Road, Cambridge CB3 0WA, UK*

⁴*Center for Computational Astrophysics, Flatiron Institute, 162 Fifth Avenue, New York, NY 10010, USA*

Accepted XXX. Received YYY; in original form ZZZ

ABSTRACT

Astrophysical objects possessing a material surface (white dwarfs, neutron stars, etc.) accrete gas from the disk through the so-called surface boundary layer (BL), in which the angular velocity of the accreting gas experiences a sharp drop. Acoustic waves excited by the supersonic shear in the BL play an important role in mediating the angular momentum and mass transport through that region. Here we examine the characteristics of the angular momentum transport produced by the different types of wave modes emerging in the inner disk, using the results of a large suite of hydrodynamic simulations of the BLs. We provide a comparative analysis of the transport properties of different modes across the range of relevant disk parameters. In particular, we identify the types of modes which are responsible for the mass accretion onto the central object. We find the correlated perturbations of surface density and radial velocity to provide an important contribution to the mass accretion rate. Although the wave-driven transport is intrinsically non-local, we do observe a clear correlation between the angular momentum flux injected into the disk by the waves and the mass accretion rate through the BL. We find the efficiency of angular momentum transport (normalized by thermal pressure) to be a weak function of the flow Mach number. We also quantify the wave-driven evolution of the inner disk, in particular the modification of the angular frequency profile in the disk. Our results pave the way for understanding wave-mediated transport in future three-dimensional, magnetohydrodynamic studies of the BLs.

Key words: accretion, accretion discs – hydrodynamics – instabilities

1 INTRODUCTION

Disk accretion onto an object possessing a material surface (i.e. not a black hole) is an important problem emerging in a variety of astrophysical settings. When the magnetic field of an accretor is weak enough (Ghosh & Lamb 1978; Koenigl 1991), the accretion flow can extend all the way to its surface. In this case the transfer of incoming matter onto the central object (hereafter "a star") must proceed through the so-called *boundary layer* (hereafter BL) — a narrow region between the disk and the accretor, in which the angular velocity of the accreting matter adjusts to the rotation of the central star. In order for that to happen, the gas arriving from the disk must lose its angular momentum inside the BL.

The magneto-rotational instability (MRI; Velikhov 1959; Balbus & Hawley 1991), traditionally invoked as the favored angular momentum transport mechanism in sufficiently ionized accretion

disks, cannot enable this process in the BL: it does not operate in this region (Pessah & Chan 2012) since the angular velocity of the fluid there necessarily *increases* with the distance. Instead, Belyaev & Rafikov (2012) proposed that a *sonic instability*, driving the excitation of acoustic waves by the supersonic shear flow inside the BL, mediates the angular momentum transport in that region in a *non-local* fashion, very different from the local α -models Shakura & Sunyaev (1973), that have been previously invoked in the BL context (Popham et al. 1993; Balsara et al. 2009; Hertfelder & Kley 2017). This instability has been subsequently verified to robustly operate within the BL and drive angular momentum transport using hydrodynamic and magneto-hydrodynamic (MHD) simulations (Belyaev et al. 2012, 2013a,b).

Recently Coleman et al. (2021) (hereafter *Paper I*) presented a new, extensive suite of two-dimensional (2D) hydrodynamic simulations of the BLs run for multiple values of the Mach number $\mathcal{M} = v_K(R_\star)/c_s$ — the ratio of the Keplerian velocity $v_K(R_\star)$ at the inner edge of the disk (i.e. at the stellar radius R_\star) to the sound speed c_s (which was assumed constant in that work). They

* E-mail: msbc@astro.princeton.edu

† John N. Bahcall Fellow at the IAS

carefully analyzed the different waves emerging in the inner disk as a result of the sonic instability operating in the BL, and discovered some new types of modes emerging in the vicinity of the BL, e.g. the vortex-driven modes. That study focused predominantly on the *morphological* characteristics of the waves and their correspondence to the known analytical results.

In this work we will use the simulation suite presented in [Paper I](#) to characterize the BL from a different angle, namely to explore the angular momentum and mass transport in its vicinity driven by the wave activity. A number of past studies explored the connection between the two transport processes in accretion disks. For example, [Balbus & Papaloizou \(1999\)](#) argued that the MRI-driven transport can be characterized as a local α -viscosity ([Shakura & Sunyaev 1973](#)), whereas the transport driven by disk self-gravity is global and cannot be represented using the α -anzatz (see also [Larson 1984](#); [Gnedin et al. 1995](#)). A number of studies have also looked at the angular momentum transport by the global spiral waves in disks ([Larson 1990](#); [Spruit 1987](#); [Rafikov 2016](#); [Arzamasskiy & Rafikov 2018](#)), in particular those driven by embedded planets [Goodman & Rafikov \(2001\)](#); [Rafikov \(2002\)](#). In the BL context, [Belyaev et al. \(2012, 2013a\)](#) explored some global transport characteristics of the acoustic waves, whereas [Belyaev et al. \(2013b\)](#) did the same in the MHD case¹. Also, [Dittmann \(2021\)](#) studied how the efficiency of transport varies as the spin of the accreting object changes.

The aim of our present work is to extend the latter studies by looking at the various characteristics of the wave-driven transport in the vicinity of the BL — angular momentum and mass fluxes — in a systematic fashion across the range of \mathcal{M} values. A distinct feature of this work compared to previous studies is that we examine the transport properties of individual modes emerging in our simulations and determine their variation across the different types of modes. Another goal is to explore the wave-driven evolution of the inner parts of the accretion disk adjacent to the BL.

This work is organized as follows. After briefly describing in §2 the simulation suite on which this study is based, we remind the reader the basics of the mass and angular momentum transport in accretion disks in §3. Our simulation results on the two kinds of transport are described in §4 and 5, respectively. We examine the different contributions to the angular momentum budget in §6 and describe the correlation between the angular momentum and mass fluxes found in our simulations in §7. The wave-driven evolution of the inner disk is characterized in §8. Finally, we discuss and summarize our results in §9 and 10, respectively.

2 DESCRIPTION OF THE NUMERICAL DATA SET

Our present study is based on the data produced by a set of 2D simulations (39 runs in total) presented in [Paper I](#). These runs used *Athena++* ([Stone et al. 2020](#)) to solve hydrodynamic equations with the globally isothermal equation of state (EOS), i.e. $P = \Sigma c_s^2$ for a constant sound speed c_s , where P is the vertically integrated pressure and Σ is the surface density. Magnetic fields and disk

¹ In their global, unstratified MHD simulations of the near-BL region [Belyaev & Quataert \(2018\)](#) found accumulation of accreted material in a belt-like structure in the BL, spinning at sub-Keplerian velocity. To allow the accreted material to join the star this belt must dissipate somehow, but it is not yet clear how that happens. Nevertheless, even with the belt [Belyaev & Quataert \(2018\)](#) still found a substantial wave activity in the inner disk, which is what matters for us in this study.

self-gravity have been ignored, and the accretor was initially non-spinning.

These simulations are set in polar $r - \phi$ coordinates, with the azimuthal coordinate covering full 2π . In the radial direction the simulation domain starts below the stellar radius R_\star and extends in the disk out to $4R_\star$. The radial grid is uniformly spaced in $\log r$ to increase resolution in the vicinity of the BL. Simulations were run for every integer value of \mathcal{M} in the interval $5 \leq \mathcal{M} \leq 15$. For three values of $\mathcal{M} = 6, 9, 12$ we run multiple simulations with the different forms of the initial noise spectrum (triggering sonic instability in the BL) and numerical resolution, to test their impact on the outcomes.

A distinctive feature of our simulations is their detailed, purpose-built, real-time analysis. They employed a high-cadence sampling of the outputs, allowing a highly informative analysis of the outputs to be performed. In particular, we ran on-the-fly fast-Fourier transforms (FFTs) of various fluid variables, giving us new, previously unobtainable diagnostic capabilities. This allowed us to detect and characterize a number of different modes present in the system, with their distinct azimuthal wavenumbers m and pattern speeds Ω_P , at every moment of time. The ability to automatically detect and analyze different modes present in the system is an important improvement of the study presented in [Paper I](#) compared to the existing works.

In the following, when presenting our results, we will be using units in which $R_\star = 1$ and $\Sigma(R_\star) = 1$ at $t = 0$; in these units the initial profile of the surface density is $\Sigma = r^{-3/2}$. We also set the Keplerian velocity at the surface of the star $v_K(R_\star)$ to be unity, which implies that $c_s = \mathcal{M}^{-1}$ and $GM_\star = 1$. This choice makes the Keplerian period at R_\star to be $\tau_\star = 2\pi$, and we will often express time in the form of $t/2\pi$, or in the units of τ_\star .

2.1 Main findings of Paper I

We now recount the main conclusions of the wave morphology study presented in [Paper I](#), that will allow us to better interpret the results of the current work.

Our suite of simulations reveals a complicated pattern of wave activity in the vicinity of the BL, with a number of different modes operating in the inner disk. In addition to the upper and lower acoustic modes previously described in [Belyaev et al. \(2013a\)](#), we have also discovered a new type of modes, so called *vortex-driven* modes. They appear as global spiral arms extending from the vicinity of the BL into the upper disk, and owe their existence to the localized vortex-like structures that form in the disk next to the BL and launch these density waves.

Another type of modes that we routinely detect in our runs are the so called *resonant* modes (owing their existence to a particular geometric resonance condition, [Belyaev et al. 2012](#)), which are present only in the disk. Similar to the lower acoustic modes, the resonant modes are trapped between the stellar surface and the inner Lindblad resonance, whose location r_{ILR} in a Keplerian disk with $\Omega = \Omega_K = (GM_\star/r^3)^{1/2}$ is given by

$$r_{\text{ILR}} = R_\star \left[\frac{\Omega_K(R_\star) m - 1}{\Omega_P m} \right]^{2/3}. \quad (1)$$

In [Paper I](#) we also found a general tendency of the azimuthal wavenumber m of the most prominent modes to increase with \mathcal{M} . These results appear robust with respect to variations of the initial conditions and numerical resolution.

3 WAVE-DRIVEN MASS AND ANGULAR MOMENTUM TRANSPORT: BASICS

The main goal of the present work is to better understand how matter and angular momentum are transported through the inner disk and the BL, resulting in accretion onto the star. To that effect, we examine how the characteristics of the different modes that we see in our runs are linked to the global evolution of the star-disk system. We do this by exploring the behavior of certain variables derived from our simulations — mass and angular momentum fluxes — for different values of \mathcal{M} and connecting them to the changes of the disk properties.

In all our simulations transport of mass is tracked by measuring the mass accretion rate,

$$\dot{M}(r) \equiv -r \int_0^{2\pi} v_r(r, \phi) \Sigma(r, \phi) d\phi = -2\pi r \langle \Sigma v_r \rangle, \quad (2)$$

(see Figure 1) where we introduced a shorthand notation

$$\langle f(r) \rangle = (2\pi)^{-1} \int_0^{2\pi} f(r, \phi) d\phi \quad (3)$$

for azimuthal averaging of any variable $f(r, \phi)$. Accretion rate is defined such that $\dot{M} > 0$ for *inflow* of mass towards the star.

To characterize angular momentum transport we adopt the standard procedure of measuring the total angular momentum flux (AMF) C_L , defined as

$$C_L = 2\pi r^2 \langle \Sigma v_r v_\phi \rangle, \quad (4)$$

where v_r and v_ϕ are the radial and azimuthal velocity components. By introducing a reference azimuthal velocity of the fluid $v_{\phi,0}(r)$, to be specified later, and the azimuthal velocity perturbation $\delta v_\phi = v_\phi - v_{\phi,0}$, we can further decompose C_L into the *advective* angular momentum flux C_A , and the *wave* angular momentum flux² (or Reynolds stress) C_S , defined as follows:

$$C_A = 2\pi r^2 \langle \Sigma v_r \rangle v_{\phi,0} = -\dot{M} r v_{\phi,0}, \quad (5)$$

$$C_S = 2\pi r^2 \langle \Sigma v_r (v_\phi - v_{\phi,0}) \rangle = 2\pi r^2 \langle \Sigma v_r \delta v_\phi \rangle, \quad (6)$$

so that $C_L = C_A + C_S$. In our case the stress contribution C_S arises primarily because of the oscillatory wave-like motions and is driven by the wave modes rather than some turbulence, as would be the case for e.g. the MRI.

In this work, when analyzing simulation outputs, we will most often be choosing $v_{\phi,0}$ to be the mean azimuthal velocity of the fluid,

$$v_{\phi,0} = \langle v_\phi \rangle, \quad (7)$$

following Fromang & Nelson (2006) and Flock et al. (2011), among others. Note that alternative definitions of C_S using other choices of $v_{\phi,0}(r)$ are also possible, see e.g. Ju et al. (2016), Arzamasskiy & Rafikov (2018), as well as §3.1.

Because of oscillatory, intrinsically time-dependent nature of the acoustic mode-driven transport, we find \dot{M} and the different angular momentum flux contributions to be highly time-dependent. For that reason, we resort to averaging these physical quantities over sufficiently long time intervals to provide meaningful comparison between them. We describe mathematical details of such averaging procedures in Appendix A.

² Despite the typographic similarities c_s and C_S are used to denote two distinct quantities: sound speed and wave-induced angular momentum flux, respectively.

3.1 Relation between \dot{M} and C_S

The mass and angular momentum fluxes through the disk are closely related to each other, which can be demonstrated quite generally starting from the hydrodynamic equations of motion and continuity. In particular, it was shown in Belyaev et al. (2013a) that by choosing $v_{\phi,0}(r)$ in the *mass-weighted* form (Balbus & Hawley 1998; Balbus & Papaloizou 1999)

$$v_{\phi,0} = v_\Sigma \equiv \frac{\langle \Sigma v_\phi \rangle}{\langle \Sigma \rangle}, \quad (8)$$

different from that given by the equation (7), and defining the wave AMF (6), or Reynolds stress, C_S accordingly (i.e. with $v_{\phi,0} = v_\Sigma$), the equation representing conservation of the angular momentum can be cast in the following form:

$$\dot{M} \frac{\partial l}{\partial r} = \frac{\partial C_S}{\partial r} + 2\pi r^3 \langle \Sigma \rangle \frac{\partial \Omega_0}{\partial t}. \quad (9)$$

Here $\Omega_0 = v_\Sigma/r$ and $l = rv_\Sigma = \Omega_0 r^2$ are the angular frequency and the specific angular momentum corresponding to the reference azimuthal velocity v_Σ . If instead of (8) we adopted $v_{\phi,0}$ in the form (7), then the last term in the equation (9) would look differently.

Equation (9) directly relates the transport of mass — the term proportional to \dot{M} in the left hand side — to the transport of the angular momentum in the disk — the divergence of the wave angular momentum flux C_S in the right-hand side. The second term in the right hand side, usually neglected in studies of accretion processes, arises in disks which evolve sufficiently rapidly for their mean angular frequency Ω_0 to change in time. If we neglect this contribution to the angular momentum balance for a moment, then we find

$$\dot{M} = \left(\frac{\partial l}{\partial r} \right)^{-1} \frac{\partial C_S}{\partial r} = \frac{\partial C_S}{\partial l}. \quad (10)$$

Note that this expression is fully general and applies for any choice of $v_{\phi,0}$; a particular form of $v_{\phi,0}$ affects the definition of both C_S and l .

In truly viscous disks with kinematic viscosity ν one should use viscous angular momentum flux $F_J = -2\pi\nu\Sigma r^3 d\Omega/dr$ instead of C_S (Lynden-Bell & Pringle 1974). In particular, in disks with radially constant \dot{M} one finds $F_J = \dot{M}l$.

However, as we will demonstrate in §6, the second term in the right hand side of equation (9) often plays an important role near the BL. This contribution to the angular momentum balance has been previously considered in Belyaev et al. (2013a), and its relation to the evolution of the disk properties was explored in Arzamasskiy & Rafikov (2018).

4 TRANSPORT OF MASS

We start by describing our results for the mass flux \dot{M} . Given that \dot{M} is closely related to C_A , see equation (5), and in the disk $v_{\phi,0}$ is typically pretty close to the Keplerian velocity (see §8.1). One can then approximate $C_A \approx -\dot{M}l_K$ outside the BL, where $l_K(r) = \sqrt{GM_\star r}$ is the specific angular momentum for a Keplerian disk. The profile of $C_A(r)$ is plotted in Figures 2-3 (blue curve in the middle row of each individual subpanel) for simulations at varied \mathcal{M} and at different moments of time. It is discussed in more details in §5.1, but for now we will mention some key features pertinent for the \dot{M} behavior.

First, in all plotted cases $C_A(r)$ (and \dot{M}) exhibits a deep minimum (maximum) close to the BL. This is naturally explained by the

enhanced wave activity near the BL, and results in important consequences for the surface density evolution in the inner disk discussed in §8. Second, in most cases both $C_A(r)$ and \dot{M} substantially diminish in amplitude far from the accretor. We will relate this behavior to the angular momentum fluxes carried by the different types of waves in §5.

4.1 \dot{M} decomposition

Our simulations reveal an interesting feature of the \dot{M} behavior near the BL, that we discuss next. Let us write down $\Sigma(r, \phi) = \langle \Sigma \rangle + \delta \Sigma(r, \phi)$, where $\delta \Sigma(r, \phi)$ is the perturbation of the surface density relative to its azimuthally-averaged value $\langle \Sigma \rangle$. Then the definition (2) can be cast as

$$\dot{M}(r) = -2\pi r \langle \Sigma \rangle \langle v_r \rangle - 2\pi r \langle \delta \Sigma v_r \rangle, \quad (11)$$

illustrating the separation of \dot{M} into two distinct contributions — the one due to the advection of the mean surface density $\langle \Sigma \rangle$ (first term) and the contribution due to the correlation between the non-axisymmetric fluctuation of Σ and v_r . We illustrate the behavior of these contributions in Figure 1 for three simulations with different values of \mathcal{M} . One can see that in all cases both contributions to \dot{M} are, in general, equally important: they are comparable in magnitude and tend to offset each other so that the total \dot{M} is considerably lower in magnitude than each of these terms over large radial ranges (which is especially noticeable near the BL). For that reason, one cannot directly connect $\dot{M}(r)$ to the radial profiles of $\langle v_r \rangle$ and $\langle \Sigma \rangle$.

Importance of the \dot{M} contribution due to the correlation between $\delta \Sigma$ and v_r is one of the distinctive features of the global, acoustic wave-driven transport. In the classical picture of laminar viscous disk accretion (Shakura & Sunyaev 1973; Lynden-Bell & Pringle 1974) this contribution is identically zero since the disk is axisymmetric and $\delta \Sigma = 0$. In our case, this contribution is non-zero in the vicinity of the BL because of highly correlated $\delta \Sigma$ and v_r for wave-like fluid motions and the nonlinear dissipation of these waves, which leads to damping of the angular momentum flux carried by the waves. Interestingly, $\langle \delta \Sigma v_r \rangle$ is often more regular than $\langle \Sigma \rangle \langle v_r \rangle$, since the latter sometimes exhibits small-scale spatial variability even upon the long-term time averaging, see Figure 1b.

We are not aware of any studies mentioning the role of the mass transport term proportional to $\langle \delta \Sigma v_r \rangle$ in simulations featuring turbulence, self-consistently driven by a local hydrodynamic (e.g. the vertical shear instability) or MHD (e.g. MRI) mechanism. Examining this issue may be interesting for figuring out whether in our case the non-zero second term in equation (11) arises due to the intrinsically global nature of the wave-driven transport near the BL (see §9.2), or it is also present when accretion is mediated by local processes.

5 ANGULAR MOMENTUM TRANSPORT

We now turn to the details of the angular momentum transport in the vicinity of the BL. Figures 2,3 illustrate the behavior of various representative variables during three different periods of time for the four representative simulations with $\mathcal{M} = 7, 9, 12$ and 15. The morphological description of the modes emerging in two of the runs — for $\mathcal{M} = 9$ (M09.FR.r.a) and $\mathcal{M} = 15$ (M15.FR.r.a) — has been provided in Paper I, whereas the $\mathcal{M} = 7$ (M07.FR.r.a) and $\mathcal{M} = 12$ (M12.FR.mix.a) runs have not been discussed in detail in Paper I.

For each \mathcal{M} we select three time intervals of length 50 or 100 orbits and perform averages (as described in Appendix A) of

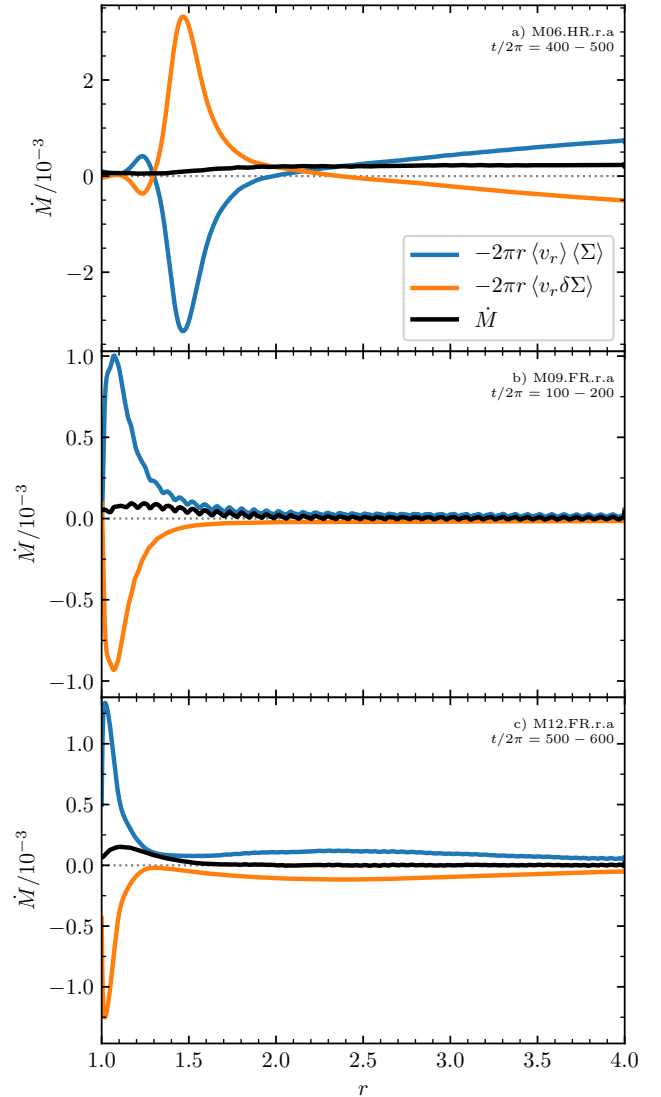


Figure 1. Different contributions to the total mass accretion rate \dot{M} (black curve) in equation (11), plotted as a function of r for several simulations (see Paper I for their naming notation). The advective term $2\pi \langle \Sigma v_r \rangle \langle v_r \rangle$ is shown in blue, while the diffusive term $-2\pi \langle \delta \Sigma v_r \rangle$ is the orange curve. Averaging over the interval $t/2\pi = 100 - 200$ is performed.

various angular momentum fluxes — total C_L , advective C_A , and wave C_S , defined by the equations (4)-(6) with $v_{\phi,0} = \langle v_{\phi} \rangle$ given by the equation (7). Their radial profiles are shown in the middle row of each panel. As mentioned earlier in §4, the behavior of the advective flux C_A in the disk is closely related to the radial profile of the mass accretion rate \dot{M} .

We also select a representative moment of time within each interval, which illustrates a set of modes typical for that period, and show snapshots of various fluid variables in the top row of the panel corresponding to that time interval. The format is the same as in Figure 2 of Paper I, namely, we show a polar map of the wave amplitude variable $rv_r\sqrt{\Sigma}$ (right), a Cartesian map of the same variable over the reduced radial range to highlight the near-BL details (middle), and a Cartesian map of the v-perturbation of orotensity $\zeta = \omega/\Sigma$ (here $\omega = \nabla \times \mathbf{v}$ is the vorticity) relative to its initial value near the BL (left).

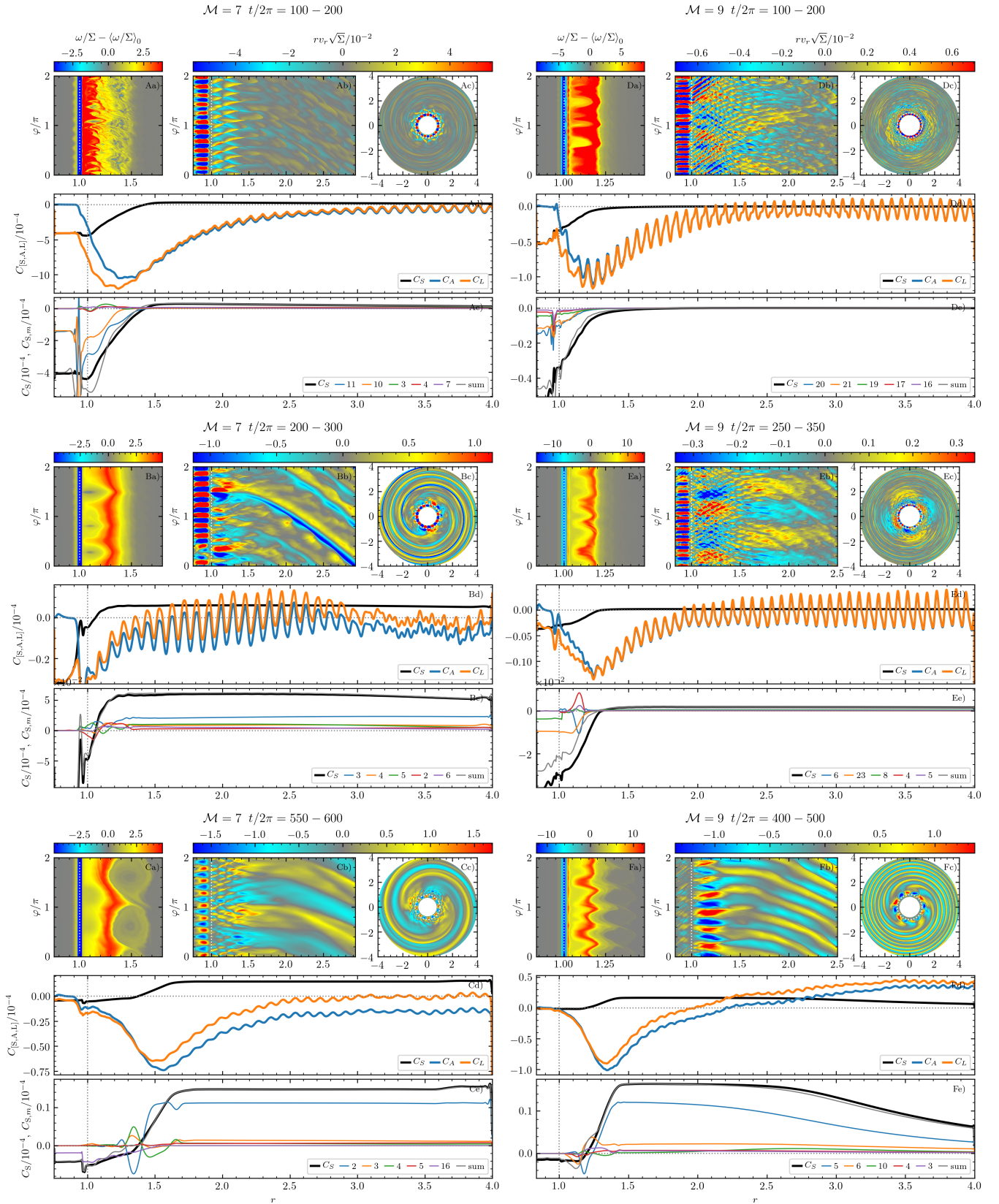


Figure 2. Figure illustrating angular momentum flux data for simulations with $\mathcal{M} = 7$ (run M07.FR.a, left panels) and $\mathcal{M} = 9$ (run M09.FR.a, right panels). Each panel (labeled with capital letters) consists of 5 sub-panels, labeled by their subscript and described in the beginning of §5. Every panel is associated with a time interval over which the AMF data are computed ($t/2\pi$, shown above the panel) and a representative moment of time $T/2\pi$ within this interval, indicated as follows.

Finally, the bottom row shows the decomposition of the wave angular momentum flux C_S into the contributions provided by the individual Fourier modes of the fluid perturbation, which are dominant through the plotted time interval (in a time integrated sense). To second order in perturbed variables the Fourier contribution $C_{S,m}$ to C_S from the m -th mode is (Belyaev et al. 2013a)

$$C_{S,m} = 2\pi r^2 \langle \Sigma \rangle \left(v_{r,m} v_{\phi,m}^* + v_{r,m}^* v_{\phi,m} \right), \quad (12)$$

where the asterisks denote complex conjugates, so that $C_S \approx \sum_{m=1}^{\infty} C_{S,m}$. The particular $C_{S,m}$ profiles shown in the figure are for the dominant modes chosen according to the procedure described in Appendix A. The gray curves, representing the sum of only the dominant harmonics indicated in each panel, sometimes show deviations from the full C_S (black), computed using equation (6). These differences arise because a number of other, less significant modes not shown in these plots also contribute to the full C_S , and also because equation (12) is only second order accurate in fluid perturbations.

The decomposition of C_S into contributions from the different azimuthal harmonics allows us to explore the role played by the individual modes (which, once their m is known, can be easily associated with the different types of waves) in transporting the angular momentum in the vicinity of the BL. This is the key advantage of our present work compared to Belyaev et al. (2013a) and Dittmann (2021), who did not perform such decomposition. Another improvement is the larger range of Mach numbers explored in our study, providing us with a better understanding of the dependence of transport properties on \mathcal{M} .

5.1 Different AMF contributions

Middle sub-panels of Figures 2-3 display the advective angular momentum flux C_A , the wave flux C_S , and their sum C_L on the same scale. A notable feature of the C_A curves is the small-scale oscillations that they often exhibit. These oscillations are likely caused by the intrinsic time-variability, since the inner disk is pervaded by the multiple wave modes. This variability ends up manifesting itself in the spatial domain, even though we perform time averaging over a substantial interval of time, see Appendix A.

One can see that $|C_A|$ peaks not too far from the stellar surface and its maximum amplitude is always larger than that of C_S by a factor of several. This makes sense since, to zeroth order (certainly in steady state), $C_A \propto \dot{M} \propto \partial C_S / \partial r$, see equations (5), (9). Since C_S typically varies over a narrow region near the BL, its radial derivative can reach high values. Naturally, the narrower is the near-BL region over which C_S varies, the larger should we expect the difference in amplitudes between C_A and C_S to be. And indeed, in Figure 2 (for $\mathcal{M} = 7$) we find C_S variation in the range $1 < r \lesssim 1.5$ to result in the ratio of the maximum amplitudes C_A and C_S being $\sim (2 - 2.5)$, while in Figure 3Fd (for $\mathcal{M} = 15$) C_S variation in the range $1 < r \lesssim 1.2$ leads to the maximum ratio of fluxes $\sim 5 - 6$.

In most cases we find C_A to be negative, as expected for mass inflow with $\dot{M} > 0$. Notable exceptions include $\mathcal{M} = 9$ run at $t/2\pi = 400 - 500$ (Figure 2Fd) and $\mathcal{M} = 15$ run at $t/2\pi = 100 - 200$ (Figure 3Dd), for which $C_A > 0$ (i.e. $\dot{M} < 0$) at large distances. This can again be understood on the basis of the equations (9) or (10), by noticing that in these cases C_S is *positive and decays* with r far from the star as a result of dissipation (it will become clear in §5.2,5.3 that this behavior is caused by the nonlinear damping of the vortex-driven modes). As a consequence, $\partial C_S / \partial r < 0$ there, leading to $\dot{M} < 0$ (outflow) and positive C_A .

5.2 Wave AMF C_S as a function of \mathcal{M} and m

We now describe the behavior of the wave AMF C_S for different values of \mathcal{M} shown in Figures 2,3 in conjunction with the morphological characteristics of the different waves present in the system.

5.2.1 $\mathcal{M} = 7$ run

We start our description of the C_S behavior with the $\mathcal{M} = 7$ run, shown in Figures 2A-C. At early times³ ($t/2\pi = 125$) the inner disk is dominated by the $m = 11$ lower mode trapped within $r \lesssim 1.5$ (panel Ab), which roughly corresponds to the r_{ILR} of this mode (its $\Omega_P \approx 0.46$). This mode gives rise to the negative AMF $C_{S,11}$, see the blue curve⁴ in panel (Ae). As a result, C_S starts negative at $r = R_*$ and crosses zero around r_{ILR} .

Outside the resonant cavity there is a set of rather incoherent vortex-driven spiral arms, excited by a number of chaotic vortices residing at $r \lesssim 1.5$, visible in panel (Aa). These weak arms drive low-amplitude but *positive* C_S outside $r = 1.5$, see panel (Ad).

By $t/2\pi = 225$ the amplitude of the wave activity decreases; $m = 11$ lower mode gets replaced with the lower $m = 10$ mode, which is prominent inside the star but is rather weak in the disk, see panel (Bb). As a result, the magnitude of the (negative) segment of the C_S curve in the inner disk drops by about two orders of magnitude, and it gets confined close to the star (panel (Bd)). Also by that time, vortensity evolution produces three prominent vortices at $r \approx 1.1$ (panel (Ba)), which excite strong vortex-driven spirals in the outer disk, increasing the amplitude of $C_S > 0$ in the outer disk (panel (Bd)).

In the final stages of this $\mathcal{M} = 7$ simulation, at $t/2\pi = 575$, a lower $m = 16$ mode clearly shows in the disk at $r \lesssim 1.8$ (although inside the star $m = 8$ mode dominates), although with rather modest amplitude (panel (Cb)). This, again, makes C_S negative close to the star, see the red curve for $C_{S,16}$ in panel (Ce). Also, the vortensity map in panel (Ca) reveals two strong, azimuthally elongated vortices centered at $r \approx 1.5$. These "rolls", as we termed them in Paper I, drive a pair of azimuthally extended vortex-driven spiral arms with $m = 2$ in the outer disk. Their $C_{S,2} > 0$ makes C_S positive in the outer disk (see panel (Ce)), with the amplitude ≈ 2.5 times higher than at $t/2\pi = 225$.

Already this run alone demonstrates that depending on a type of the mode dominating in a particular region of the disk, one can get rather different behaviors of C_S . Our subsequent description of the runs for other values of \mathcal{M} will reinforce this conclusion.

5.2.2 $\mathcal{M} = 9$ run

The $\mathcal{M} = 9$ run in its early phases $t/2\pi = 150$ reveals a set of lower $m = 19 - 21$ modes confined within $r_{\text{ILR}} \approx 2.2$, corresponding to their $\Omega_P \approx 0.3$, see Figure 2Db, Dc. These modes give rise to $C_S < 0$ near the star. Similar picture persists also at $t/2\pi = 275$, see panels (Eb)-(Ee). At the same time, in the outer disk C_S stays close to zero: unlike the late stages of the $\mathcal{M} = 7$ run, coherent vortices

³ Note that by that time a significant depression in surface density has already formed in the inner disc, see Figure 4a.

⁴ The orange curve in that panel corresponding to the $m = 10$ lower mode also provides a substantial contribution to C_S near the star. This mode is not seen in panels (Aa)-(Ac) because the data shown in panels (Ad), (Ae) are integrated over an extended time interval and $m = 10$ signal gets washed out.

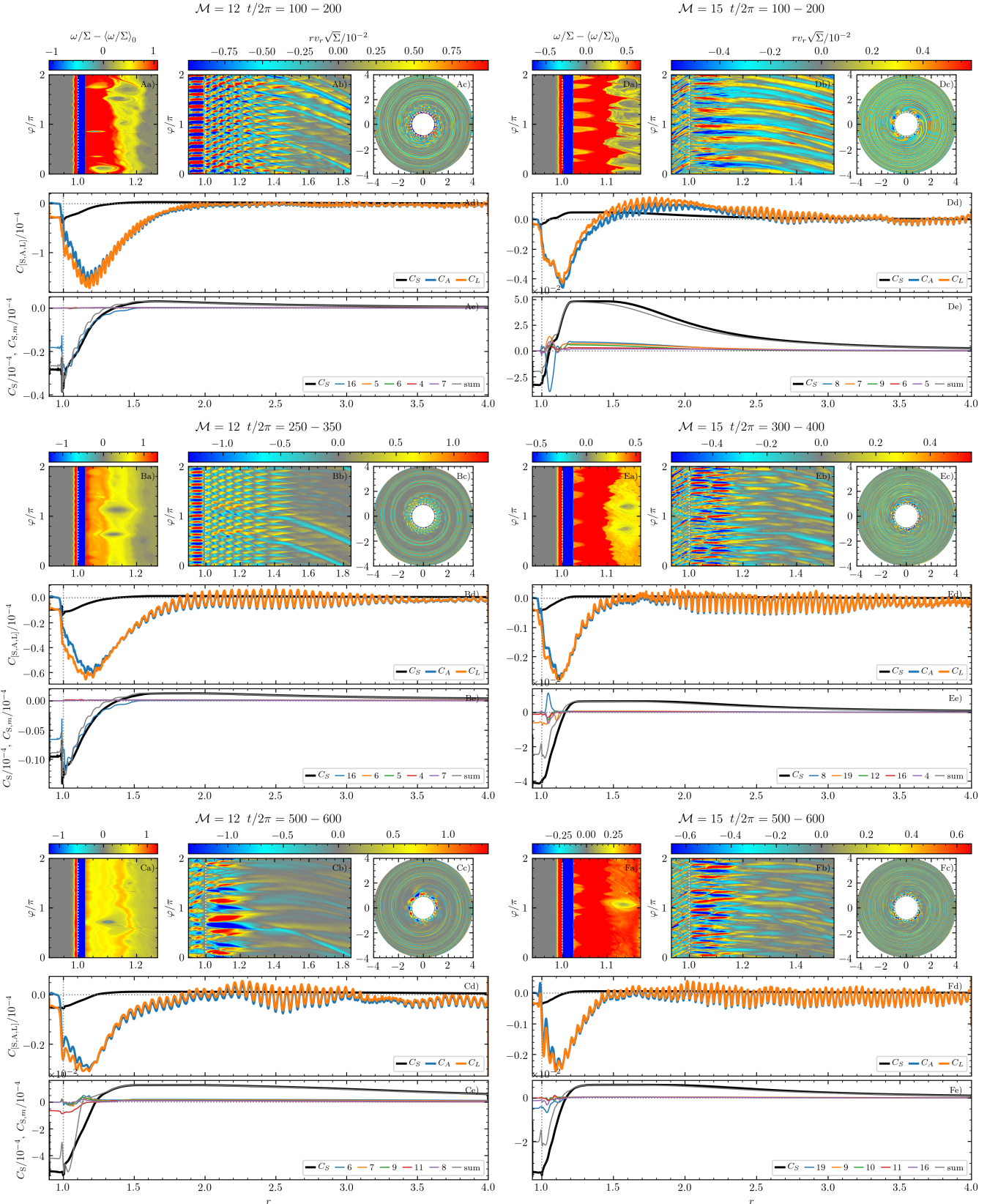


Figure 3. Same as Fig. 2 but for $M = 12$ (run M12.FR.mix.lc.a, left panels) and $M = 15$ (run M15.FR.r.a, right panels). For $M = 12$: (A) $T/2\pi = 150$, $t/2\pi = 100 - 200$; (B) $T/2\pi = 300$, $t/2\pi = 250 - 350$; (C) $T/2\pi = 575$, $t/2\pi = 550 - 600$. For $M = 15$: (D) $T/2\pi = 150$, $t/2\pi = 100 - 200$; (E) $T/2\pi = 350$, $t/2\pi = 300 - 400$; (F) $T/2\pi = 550$, $t/2\pi = 500 - 600$.

do not emerge near the star (see panels (Da), (Ea)), so vortex-driven spirals are very weak.

An interesting feature of the $\mathcal{M} = 9$ run pointed out in [Paper I](#), is the emergence of $m = 2$, radially elongated mode with very low pattern speed $\Omega_P \approx 0.15$. It is readily noticeable in panel (Eb), however its signal is not present in panel (Ee), which means that its AMF contribution $C_{S,2}$ is negligible. This is hardly surprising since this mode has radial wave number $k_r = 0$.

Finally, at $t/2\pi = 150$ the picture changes dramatically, see panels (Fb),(Fc). Near the star, for $r \lesssim 1.4$, the disk is dominated by the $m = 6$ resonant mode (see [Paper I](#) for details), whereas in the outer disk there are global $m = 5$ spiral arms driven by a set of five vortex rolls located at $r \approx 1.3$, see panel (Fa). The resonant mode gives rise to a small (but negative near the star) AMF contribution $C_{S,6}$, whereas the vortex-driven modes produce $C_{S,5} > 0$ in the outer disk, similar to $\mathcal{M} = 7$ run.

5.2.3 $\mathcal{M} = 12$ run

An $\mathcal{M} = 12$ run that we use in this work is different from the run employed in [Paper I](#). This is done in part to illustrate the fact, pointed out in [Paper I](#), that all $\mathcal{M} = 12$ runs look very similar to each other, in a much more homogeneous way than for any other value of \mathcal{M} .

Indeed, comparing Figure 3A-C with the Fig. 7 of [Paper I](#), one can see a very familiar pattern: for most of the simulation, including $t/2\pi = 150$ and 300 shown in Figure 3A,B, the inner disk (out to $r \approx 1.6$) is dominated by the lower $m = 16$ mode, accompanied by a set of narrow vortex-driven spirals clearly visible in the outer disk. As expected, this pattern results in $C_{S,16}$ driving $C_S < 0$ near the star, with C_S becoming positive further out, at $r \gtrsim 1.3 - 1.5$, see panels (Ae), (Be).

Closer to the end of the run, at $t/2\pi = 550$, one can see a combination of a resonant and a lower $m = 11$ modes driving C_S below zero near the star, with the weak vortex-driven modes carrying $C_S > 0$ outside $r \approx 1.3$.

5.2.4 $\mathcal{M} = 15$ run

The $\mathcal{M} = 15$ simulation is the highest \mathcal{M} run carried out as a part of our simulation suite described in [Paper I](#). Unlike other simulations described so far, this run shows quite substantial upper acoustic mode activity inside the star ([Belyaev et al. 2013a](#)), see Figure 3Db,Eb,Fb, although the manifestations of this mode type in the disk are not as clear.

In this run we witness the appearance of 7-8 vortex rolls at $r \approx 1.15$ rather early on, already by $t/2\pi = 150$, see panel Da. These rolls drive a set of global, relatively narrow spiral arms propagating in the outer disk and making C_S positive beyond $r \approx 1.1$. For $1 < r \lesssim 1.1$ we find $C_S < 0$, which could be due to the resonant modes starting to develop in this part of the disk.

These resonant modes do become rather prominent (and more radially extended) at later time, e.g. at $t/2\pi = 350$ and 550, see panels (Eb),(Fb). They keep C_S negative within $r \approx 1.2$, see panels (Ee),(Fe). At the same time, the vortex rolls appearing earlier in the simulation merge into two (at $t/2\pi = 350$) and then one vortex (at $t/2\pi = 550$), see panels (Ea), (Fa). They give rise to the vortex-driven mode activity in the outer disk, which maintains positive C_S there, albeit at a reduced amplitude compared to $t/2\pi = 150$.

5.3 Transport by the different types of modes

Examination of the bottom sub-panels in all panels of Figures 2-3 reveals that at any moment of time there is often only one or two modes in the disk that dominate the wave AMF C_S . For example, in the $\mathcal{M} = 7$ run at $t/2\pi = 100 - 200$ we find two lower modes with $m = 10, 11$ to provide the dominant contribution to C_S for $r < 1.4$ (Figure 2Ae), while at $t/2\pi = 550 - 600$ the vortex-driven $m = 2$ mode dominates C_S for $r > 1.4$ (Figure 2Ce); in the $\mathcal{M} = 12$ run the lower $m = 16$ mode dominates C_S for $r < 1.5$ at both $t/2\pi = 100 - 200$ and 250 - 350 (Figure 3Ae,Be). As these dominant modes have a particular sign of C_S , they affect disk evolution in a certain way, as described later in §8.

A wave propagating in the disk carries angular momentum $\Delta J_w \propto [\Omega_P - \Omega(r)]$ (see below), so that the flux of angular momentum associated with it is

$$C_S \propto k_r \Delta J_w \propto k_r [\Omega_P - \Omega(r)], \quad (13)$$

where k_r is the radial wavenumber. In particular, an outgoing ($k_r > 0$) wave has $C_S > 0$ in the region where $\Omega_P > \Omega(r)$ (e.g. a vortex-driven mode far from the star), whereas an incoming ($k_r < 0$) wave has $C_S > 0$ in the region where $\Omega_P < \Omega(r)$ (e.g. a lower mode reflected off the ILR). This is what one also finds for the density waves excited by planets, outside and inside of the planetary semi-major axis. On the other hand, in the disk region where $\Omega_P < \Omega(r)$ an outgoing ($k_r > 0$) wave has $C_S < 0$ (e.g. a lower mode propagating away from the star).

Nonlinear wave damping provides an intuitive way to understand why $\Delta J_w \propto \text{sgn}[\Omega_P - \Omega(r)]$. Let us consider a shock wave with a pattern speed Ω_P . Whenever $\Omega_P > \Omega(r)$ (which is true far from the accretor) the shock overtakes the disk fluid, *accelerating* it in the azimuthal direction upon crossing the shock as a result of the shock jump conditions. As a result, disk fluid receives *positive* ΔJ from the wave. On the contrary, for $\Omega_P < \Omega(r)$ (fulfilled close to the BL, in the inner disk) the disk fluid catches up with the shock front and *decelerates* upon crossing it; this means that the wave has transferred *negative* angular momentum to the disk, i.e. that $\Delta J_w < 0$.

5.3.1 Transport by the lower acoustic modes

Lower modes are trapped inside the resonant cavity at $1 < r < r_{\text{ILR}}$, and in this part of the disk $\Omega_P < \Omega(r)$. The mode is excited in the BL ([Belyaev et al. 2013a](#)) and first propagates out (i.e. $k_r > 0$) towards the ILR. At the ILR (where its $k_r \rightarrow 0$) it gets reflected and propagates back to the stellar surface with $k_r < 0$ (see Figure 3Ab for an illustration). As a result, the outgoing lower mode has angular momentum flux $C_S^{\text{out}} < 0$, whereas the incoming (reflected) one carries $C_S^{\text{in}} > 0$. The full angular momentum flux is the sum of the two,

$$C_S(r) = C_S^{\text{out}}(r) + C_S^{\text{in}}(r). \quad (14)$$

Because of the nonlinear wave damping, $|C_S^{\text{out}}(r)|$ gradually decreases in amplitude as r increases, whereas $|C_S^{\text{in}}(r)|$ decreases in amplitude with decreasing r . As a result, for any $1 < r < r_{\text{ILR}}$ one finds that the negative $C_S^{\text{out}}(r) < C_S^{\text{out}}(r_{\text{ILR}})$, whereas the positive $C_S^{\text{in}}(r) < C_S^{\text{in}}(r_{\text{ILR}})$. Also, $C_S^{\text{out}}(r_{\text{ILR}}) = -C_S^{\text{in}}(r_{\text{ILR}})$ since $C_S(r_{\text{ILR}}) = 0$. With this in mind, equation (14) can be cast as

$$C_S(r) = [C_S^{\text{out}}(r) - C_S^{\text{out}}(r_{\text{ILR}})] + [C_S^{\text{in}}(r) - C_S^{\text{in}}(r_{\text{ILR}})] < 0, \quad (15)$$

showing that C_S of the lower modes is always negative, in agreement

with Figures 2-3. As a result, these modes drive mass flow towards the accretor, $\dot{M} > 0$, see §8.

5.3.2 Transport by the resonant modes

Resonant modes are very similar to the lower modes, since they are also trapped in the resonant cavity, where $\Omega_P < \Omega(r)$. They also propagate both towards and away from the ILR. As a result, by applying the same logic as in §5.3.1, we conclude that resonant modes have $C_S(r) < 0$ and their dissipation gives rise to $\dot{M} > 0$.

Typically, the magnitude of C_S for the resonant modes is lower than $|C_S|$ of the lower modes. This is caused by the smaller azimuthal wavenumber m of the resonant modes: lower m implies azimuthally wider wave profile, slower nonlinear wave steepening and shocking, and weaker dissipation. As a result, for resonant modes $C_S^{\text{out}}(r)$ and $C_S^{\text{in}}(r)$ in equation (14) are closer in amplitude to each other (but still different in sign) than for the lower modes, resulting in their more substantial cancellation and lower $|C_S|$.

5.3.3 Transport by the vortex-driven modes

Vortex-driven modes have Ω_P set by the angular frequency of their parent vortices, which is typically high since the vortices reside not too far from the BL. As a result, these modes propagate with $k_r > 0$ and $\Omega_P > \Omega(r)$ in the outer disk, *outside* the corotation region of the mode. This means that these modes have $C_S > 0$ and (in steady state) result in $\dot{M} < 0$, i.e. mass *outflow* in the outer disk.

As shown in Paper I, vortex-driven waves typically fall into two classes: those produced by the compact, isolated vortices (e.g. see Figure 2Ba,Bb,3Aa,Ab), and the ones driven by the more azimuthally elongated "rolls" (e.g. see Figure 2Ca,Cb,Fa,Fb). The former have small azimuthal width and are superpositions of a number of high- m perturbation modes (see Paper I). As a result, their constituent modes are often not singled out individually in our plots, see e.g. the $C_S > 0$ segments in the outer disk in Figures 2Be,3Ae, which are not dominated by a mode with a single value of m . On the contrary, the azimuthally extended rolls typically produce waves with a well defined, low value of m . As a result, in such cases a particular $C_{S,m}$ dominates the full C_S in the outer disk, see Figures 2Ce,Fe.

The way in which vortex-driven modes dissipate depends on their amplitude, as well as \mathcal{M} and m . Higher m accelerates wave evolution into a shock because of the smaller azimuthal scale. For that reason, the vortex-driven $m = 2$ mode in the $\mathcal{M} = 7$ run shown Figure 2Ce experiences little damping (its $C_{S,2}$ is essentially constant in the outer disk), whereas the $m = 5$ vortex-driven mode in the $\mathcal{M} = 9$ run shown Figure 2Fe starts damping appreciably outside $r \approx 2.5$. Note that these modes have similar \mathcal{M} and amplitude, so it is the difference in their m that is responsible for the difference in their decay. Also, everything else being equal, higher amplitude and higher \mathcal{M} (Goodman & Rafikov 2001; Rafikov 2002) of a wave promote its faster shocking and dissipation.

5.3.4 Transport by the upper acoustic modes

Upper acoustic modes show up in the disk early on in low \mathcal{M} runs. At high \mathcal{M} they also operate inside the star over long periods of time, see Paper I. These modes are evanescent near the BL, where their $\Omega_P < \Omega(r)$, but become propagating outside their Outer Lindblad Resonance, where their $\Omega_P > \Omega(r)$. In that regard, they are similar to the vortex-driven modes considered above, meaning that they

promote mass outflow in the disk, $\dot{M} < 0$. However, the amplitude of the \dot{M} driven by these modes in the disk is typically too low to make them a significant agent in the disk evolution.

5.3.5 Transport by other modes

Another interesting mode type that we see in our simulations is the low $m = 2$ mode in $\mathcal{M} = 9$ runs clearly visible in Figure 2Eb. This mode has a characteristic radially elongated perturbation pattern (with a clear shift of phase around $r \approx 1.5$) with $k_r = 0$. This implies that this mode propagates purely azimuthally and thus does not transport angular momentum in the radial direction. This conclusion is supported by the lack of $C_{S,2}$ among the different $C_{S,m}$ appearing in Figure 2Ee.

5.4 Effective transport coefficients

A standard way of quantifying transport processes in an accretion disc is through the use of the dimensionless α parameter, which effectively normalizes stress by the thermal pressure Σc_s^2 (Shakura & Sunyaev 1973). If the stress is caused by some form of local shear viscosity (e.g. due to MRI turbulence), then the same α also characterizes mass accretion through the disk. However, the transport of mass and energy associated with the acoustic modes is intrinsically non-local as sonic waves are dissipated far from their launching site. Nevertheless, we can still formally define the two dimensionless quantities based on Reynolds stress associated with the wave angular momentum flux C_S and accretion mass flux \dot{M} as follows:

$$\alpha_{\text{stress}} \equiv \frac{C_S}{2\pi r^2 \Sigma c_s^2} = \frac{C_S}{2\pi r^2 \Sigma} \left[\frac{\mathcal{M}}{v_K(R_\star)} \right]^2, \quad (16)$$

$$\alpha_{\text{acc}} \equiv \frac{\dot{M}}{2\pi \Sigma c_s^2} \Omega = \frac{\dot{M}}{2\pi \Sigma} \left[\frac{\mathcal{M}}{v_K(R_\star)} \right]^2 \Omega. \quad (17)$$

Using equation (10) we can also write α_{acc} as

$$\alpha_{\text{acc}} = \frac{\Omega}{2\pi \Sigma} \left[\frac{\mathcal{M}}{v_K(R_\star)} \right]^2 \left(\frac{\partial l}{\partial r} \right)^{-1} \left[\frac{\partial C_S}{\partial r} + 2\pi r^3 \langle \Sigma \rangle \frac{\partial \Omega_0}{\partial t} \right] \quad (18)$$

$$= \frac{\Omega}{2\pi \Sigma} \left[\frac{\mathcal{M}}{v_K(R_\star)} \right]^2 \left(\frac{\partial l}{\partial r} \right)^{-1} \frac{\partial C_S}{\partial r} \quad \text{in steady state.} \quad (19)$$

Any local transport mechanism acting as a source of shear viscosity would naturally have $\alpha_{\text{stress}} = \alpha_{\text{acc}}$, but in our case of the transport being global this is no longer true. We illustrate this difference in Figure 4, where we show α_{stress} (middle row) and α_{acc} (bottom row) as a function of time and radial location in the vicinity of the stellar surface for several values of \mathcal{M} . This data has also been box-car smoothed in the time dimension only, with a width of $\delta t/2\pi = 5$.

First, one can see that in many cases α_{stress} and α_{acc} are different not only in magnitude but also in sign, in drastic difference with the Shakura & Sunyaev (1973) model. In particular, for all \mathcal{M} we find α_{acc} to be positive over extended intervals of time and space, while α_{stress} is negative (clearly visible for $t/2\pi \lesssim 200$, $r < 1.4$ in $\mathcal{M} = 7$ case, almost always in the $\mathcal{M} = 12$ case, and so on). Comparison with the Figures 2,3 shows that this situation is typical whenever the parts of the disk adjacent to the star are dominated by the modes trapped in the resonant cavity near the star — lower and resonant modes — which carry $C_S < 0$ and have large $\partial C_S/\partial r > 0$. This naturally results in $\alpha_{\text{stress}} < 0$ and $\alpha_{\text{acc}} > 0$, see equations (16)-(19).

Further from the star, the disk is typically dominated by the

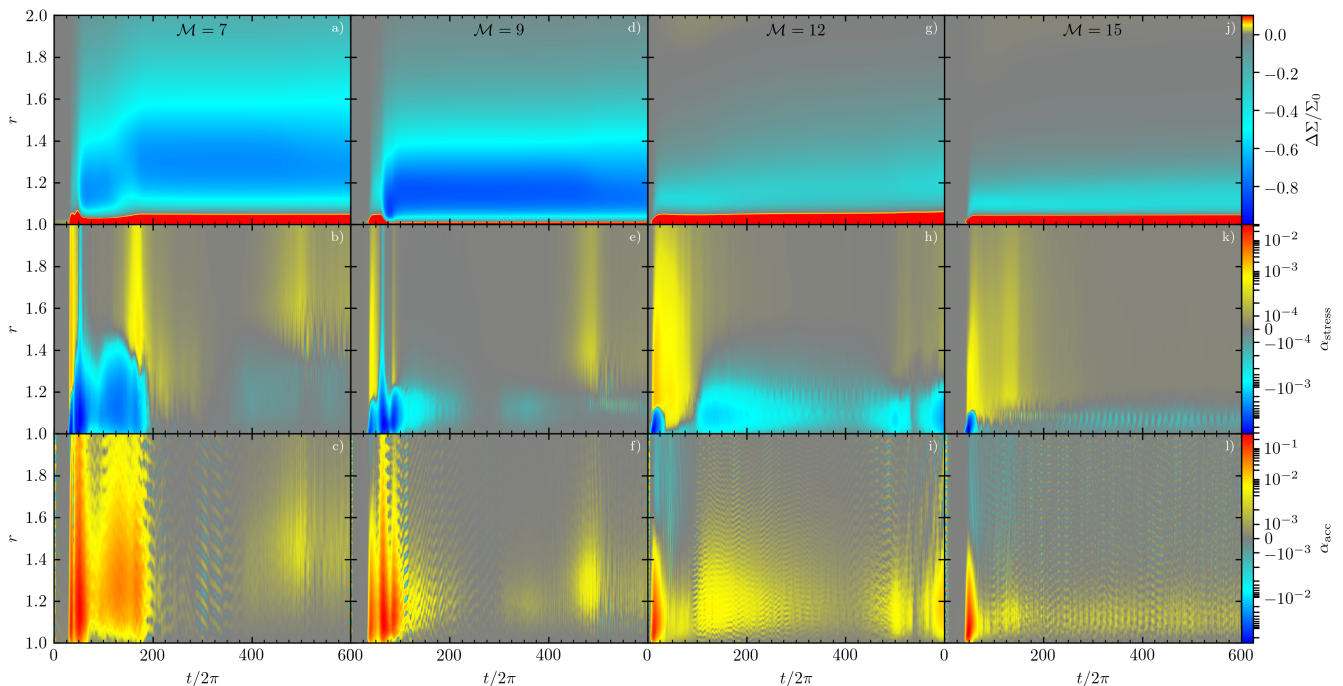


Figure 4. Space-time diagrams of $(\Sigma(t) - \Sigma(0))/\Sigma(0)$ (top), α_{stress} (middle), and α_{acc} (bottom), defined by equations (16)-(17) for the four simulations described in §5. Note that the two α parameters often have different signs, even though their amplitudes vary in similar fashion (with ‘bursts’ over the same time intervals). Large values of α typically lead to significant depletion of material from the disk. See text for details.

upper and vortex-driven modes carrying low-amplitude $C_S > 0$, which results in $\alpha_{\text{stress}} > 0$. As for α_{acc} , we find it to be negative in some cases, e.g. at $t/2\pi \lesssim 100$ in $M = 12$ case, or at $t/2\pi \sim 100$ in $M = 15$ case, when strong vortex-driven modes are present for $r \gtrsim 1.5$. This situation is typical when $C_S > 0$ carried by the upper or vortex-driven modes decays sufficiently rapidly with r (as a result of nonlinear dissipation), leading to large $\partial C_S / \partial r < 0$ and mass outflow, see (18)-(19). But more often we find $\alpha_{\text{acc}} > 0$ even far from the star, despite C_S being positive there (e.g. for $t/2\pi \lesssim 200$ in $M = 7$ case). This may seem surprising, since $\partial C_S / \partial r$ is typically small but negative during such episodes, see Figure 3Be, which would result in mass outflow according to the equation (19). However, this steady-state equation does not apply in such situations, as the (second) time-dependent term in the brackets in equation (18) is often more important than the (negative) divergence of C_S , driving mass inflow and $\alpha_{\text{acc}} > 0$ even far from the star.

Second, both α_{stress} and α_{acc} are clearly highly variable both in time and space. This has important implications for the mediation of accretion flow by the modes, which will be discussed in §9.1. The peak values of α_{stress} and α_{acc} are reached during the relatively short-lived bursts of activity. Outside of these episodes both $|\alpha_{\text{stress}}|$ and $|\alpha_{\text{acc}}|$ can maintain much lower levels $\lesssim 10^{-3}$ for extended periods of time.

Third, with our data we can compare the values of α typical for simulations with different M . One can see that α_{stress} varies roughly from -10^{-2} to 10^{-3} , with negative (positive) values marking the local dominance of either lower or resonant (upper or vortex-driven) modes. At the same time, α_{acc} only rarely attains negative values (at the level of -10^{-3}) implying mass outflow. Its peak amplitude can be as high as ~ 0.1 when it is positive. Results shown in Figure 4 suggest that α_{stress} and α_{acc} do not show any obvious dependence on M . These transport parameters certainly show little variation

with M at higher \dot{M} , e.g. during the bursts of activity confined to relatively short intervals in the beginning of each simulation. This observation is important since it suggests that similar values of α_{stress} and α_{acc} may be expected also for significantly higher M , typical for many astrophysical objects, see Paper I.

High amplitudes of α_{stress} and α_{acc} during the initial phases of our simulations lead to rapid re-adjustment of the disk structure in response to the vigorous deposition of the angular momentum carried by the waves, as described in §8. The top row of Figure 4 illustrates this process by showing the space-time diagram of the local surface density change in the disk. It is clear that injection of angular momentum by the acoustic modes into the inner disk leads to the depletion of gas in the disk out to $r \sim (1.2 - 1.6)$, which gets accreted onto the central object. The depletion usually takes place early on, following the large bursts of α_{acc} .

There is also an inverse effect: a significant depletion of mass in the inner disk Figure 4 acts to suppress the mode amplitudes and to reduce the efficiency of the angular momentum and mass transport. This is quite clear in the $M = 7, 9$ simulations, where the amplitudes of α_{stress} and α_{acc} sharply drop right after a substantial gap has been carved up in the inner disk during the initial burst of accretion. In our purely hydrodynamic simulations, there is no mechanism (e.g. MRI) to replenish this accreted material. As a result, we do not achieve a true steady state. However, situation would be different when other transport mechanisms operating in the bulk of the disk are taken into account, see §9.1.

6 DETAILED ANGULAR MOMENTUM BALANCE

Next we examine the role played by the different contributions in the angular momentum balance equation (9). In Figure 5 we plot

the time averages (see Appendix A for details of the averaging procedure) of the three terms featured in that equation, computed for $v_{\phi,0} = v_{\Sigma}$ (see equation (8)), for three different simulations ($\mathcal{M} = 6, 9, 12$) listed in the figure. One can see that in all runs the sum of the two terms in the right-hand side of the equation (9), represented by the red dotted curve, falls right on top of the black $\dot{M}\partial_r l$ curve, as expected. This demonstrates that the relation (9) indeed holds with high accuracy in our simulations.

In most cases \dot{M} (as well as $\dot{M}\partial_r l$, which is plotted) is positive (meaning inflow) and largest near the star, for $r \lesssim 1.5$. This behavior can often be directly related to that of C_{Σ} , e.g. see Figures 2Be, 3Ae,Aj, in which the positive radial derivative of C_{Σ} provides the dominant contribution to the right hand side of the equation (9) near the star. Large $\partial_r C_{\Sigma} > 0$ leading to large \dot{M} arises in the inner disk because of the deposition of the AMF carried by the lower and resonant modes, which are trapped in the resonant cavity near the star. On the other hand, at larger radii one can also find low-amplitude $\dot{M} < 0$, meaning outflow, see Figure 5b at $r \gtrsim 2.5$ and §5.4.

Very importantly, one can see that in all cases shown in Figure 5 the last term in equation (9) accounting for the time-dependence of the mean rotational profile in the disk (marked $\partial_t v_{\phi}$ for brevity) plays a very significant role. In many cases its contribution (orange curve) is similar in amplitude (but opposite in sign) to that of $\partial_r C_{\Sigma}$, see e.g. Figure 5a,b. At first, this may seem rather surprising since the variation of Ω during the corresponding time intervals is quite small (see Figure 8). However, it must be also kept in mind that all terms in equation (9) are *second-order* in perturbed variables and are thus small in magnitude. For that reason, even a weak variation of Ω in time can provide a substantial contribution to the angular momentum balance in equation (9). We will discuss the implications of this observation in §9.1.

7 C_{Σ} - \dot{M} CORRELATION

A classical steady-state accretion disk with no torque at the origin, which is mediated by the local shear viscosity necessarily exhibits a linear scaling between the *instantaneous, local* values of the viscous angular momentum flux C_{Σ} and \dot{M} in the form $C_{\Sigma} = \dot{M}l_K$, where l_K is the Keplerian angular momentum. The non-local wave-driven transport that we observe in our BL simulations does not need to obey the same relation, for several reasons. First, the angular momentum balance in equation (9) involves the time-dependent term, which is generally non-zero, see §6. Second, even in steady state equation (10) provides only a differential relation between C_{Σ} and \dot{M} ; solving for C_{Σ} would require the knowledge of its value at the boundary $r = R_{\star}$, which is not necessarily zero (as we show next).

Nevertheless, the overall amplitude of \dot{M} should still correlate somehow with the amplitude of C_{Σ} , an expectation based on the equation (9). To check whether this is the case we performed the measurement of C_{Σ} and \dot{M} at the stellar surface, i.e. $C_{\Sigma}(R_{\star})$ and $\dot{M}(R_{\star})$. The radius $r = R_{\star}$ is chosen so as to minimize the impact of wave damping and non-uniformity of \dot{M} in the disc on the measurement of angular momentum and mass fluxes. This measurement is quasi-simultaneous, since we average these quantities over 5 or 10 inner orbits to reduce the stochastic noise, which is naturally present near the BL. The results are plotted in Figure 6 for the $\mathcal{M} = 9$ and $\mathcal{M} = 12$ runs previously discussed in §5.2.2,5.2.3.

There are several notable features in these plots. First, $C_{\Sigma}(R_{\star})$ is almost always negative, which is consistent with the $C_{\Sigma}(r)$ behav-

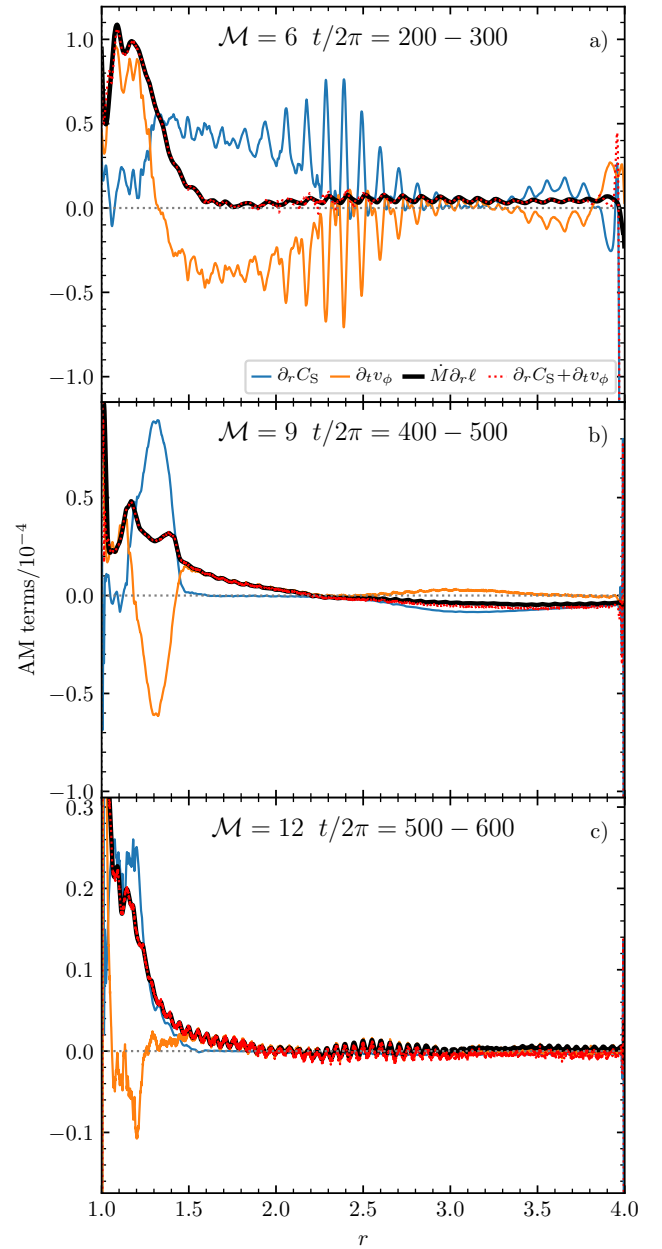


Figure 5. Different terms in the angular momentum balance equation (9) extracted from our simulations. Blue ($\partial_r C_{\Sigma}$), orange (denoted as $\partial_t v_{\phi}$) and black ($\dot{M}\partial_r l$) curves correspond to the second, third and first terms in this equation, respectively (see the legend). Red dotted curve gives the sum of the blue and orange curves, which should equal the black one in theory (as it does). Appropriately averaged (see Appendix A for details) data are shown for 3 runs: (a) $\mathcal{M} = 6$ (run M06.HR.r.a) for $t/2\pi = 200 - 300$; (b) $\mathcal{M} = 9$ (run M09.FR.r.a) for $t/2\pi = 400 - 500$; (c) $\mathcal{M} = 12$ (run M12.FR.mix.a) for $t/2\pi = 500 - 600$.

ior in Figures 2,3. Second, for moderate negative values of $C_{\Sigma}(R_{\star})$ one often observes values of \dot{M} , which are roughly equal in magnitude but opposite in sign. This is most likely caused by the oscillatory nature of the wave driven transport activity near the BL (note that Figure 6 uses quasi-logarithmic scale).

Third, and most importantly for us, the largest negative values of $C_{\Sigma}(R_{\star})$ are very tightly correlated with the largest positive

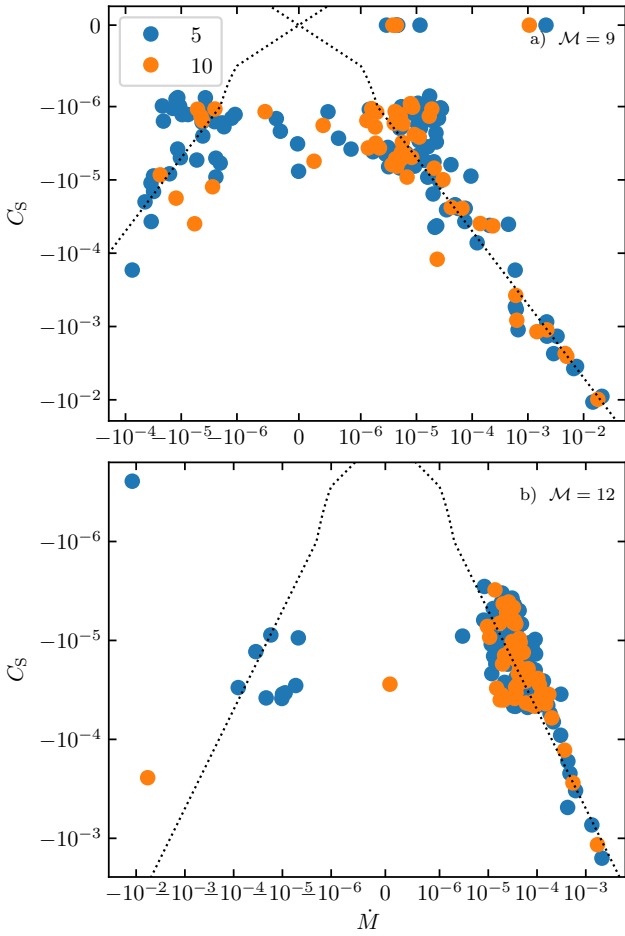


Figure 6. Correlation between the time-averaged values of C_S and \dot{M} for two runs: (a) $\mathcal{M} = 9$ run M09.FR.r.a and (b) $\mathcal{M} = 12$ run M12.FR.mix.a. Dots show the time-averaged data taken at different moments of time, with color showing the duration of time-averaging interval: 5 (blue) or 10 (yellow) orbits. The dotted black lines are $C_S = \pm 0.5\dot{M}$ to illustrate equation (20).

values of $\dot{M}(R_\star)$. We quantified this correlation by examining the dimensionless quantity C_S/\dot{M} (in simulation units, with $R_\star = 1$, $v_K(R_\star) = 1$) in every run of our simulation suite described in Paper I. To evaluate this ratio, we averaged $C_S(R_\star)$ and $\dot{M}(R_\star)$ separately in time over five orbits for each simulation⁵. Part of the reason for this averaging⁶ is to smooth over possible time lags between $C_S(R_\star)$ and $\dot{M}(R_\star)$ arising due to the nonlocal nature of the wave driven transport. This data is plotted in Figure 7, and results in (median \pm one quartile)

$$\left. \frac{C_S}{\dot{M}\ell_K} \right|_{r=R_\star} = -0.51^{+0.28}_{-0.17}. \quad (20)$$

This relation (shown with dotted lines in Figures 6,7) once again demonstrates that mass inflow into the BL requires *negative* C_S at the stellar interface. It also characterizes the efficiency with which mass accretion is enabled by the angular momentum injection into

⁵ We also tried using 10 orbits for averaging interval and found that the results were consistent to within 10%.

⁶ We discard some bins to remove the initial data and noisy data in which both quantities frequently change sign.

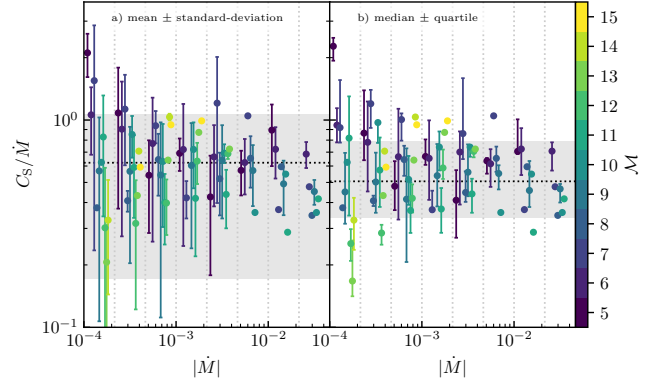


Figure 7. The ratio of C_S/\dot{M} at $r = R_\star = 1$ (in simulation units, equal to $C_S/(\dot{M}\ell_K)|_{r=R_\star}$ in physical units) as a function of \dot{M} , with the color denoting the value of \mathcal{M} of the runs from the data were taken. Each colored point represents a sample of five orbit period averages of data for the corresponding \mathcal{M} , such as blue dots shown in Fig. 6, and the statistical properties of that sample: in panel (a) we show means \pm one standard-deviation and in (b) we show medians \pm one quartile. The data are binned in \dot{M} prior to constructing the sample, the vertical dotted grey lines indicate the bins. Horizontal placement of points within a bin is not meaningful; the points are spread out so that they do not visually overlap. Points without error bars correspond to samples consisting of a single five orbit period average. The horizontal black dotted line and shaded grey band show the global mean/median \pm one standard-deviation/quartile for (a)/(b) respectively.

the disk by the wave modes excited in the BL. Finally, it provides an important boundary condition, which can be used in constructing semi-analytical models describing the structure of the inner regions of accretion disks fully or partly mediated by the acoustic waves.

8 WAVE-DRIVEN DISK EVOLUTION

In the absence of wave damping C_S would be exactly conserved in our globally isothermal setup, implying no transfer of the wave angular momentum to the disk and $\dot{M} = 0$. But in our simulations wave modes of different types can exchange their angular momentum with the disk fluid, causing its surface density to evolve. Since our runs have no viscous or radiative dissipation, this exchange is accomplished through the nonlinear dissipation of the waves (Goodman & Rafikov 2001; Rafikov 2002): nonlinear steepening of the acoustic wave profile eventually turns the wave into a shock (Landau & Lifshitz 1959), transferring its angular momentum to the background flow (Rafikov 2016). This process inevitably occurs even if the shock is weak.

Nonlinear damping always *reduces* wave amplitude and $|C_S|$, regardless of the sign of C_S . As a result, in agreement with the equations (9)-(10), non-zero \dot{M} arises in the disk changing its structure. But the direction of the mass flow also depends on a particular type of the wave and, more specifically, on the sign of AMF C_S that it carries.

As we saw in §5.4, damping of the modes with $C_S < 0$, e.g. lower and resonant modes (see §5.2), gives rise to $\partial C_S/\partial t \propto \partial C_S/\partial r > 0$, leading to $\dot{M} > 0$ (see equations (9),(10)), i.e. mass *inflow* through the disk. On the other hand, dissipation of the modes with $C_S > 0$, i.e. the upper and vortex-driven modes, can sometimes lead to $\partial C_S/\partial t > 0$. As a result, the disk fluid gains angular momentum, resulting in $\dot{M} < 0$, i.e. mass *outflow*.

In practice, lower and resonant modes carrying $C_S < 0$ gen-

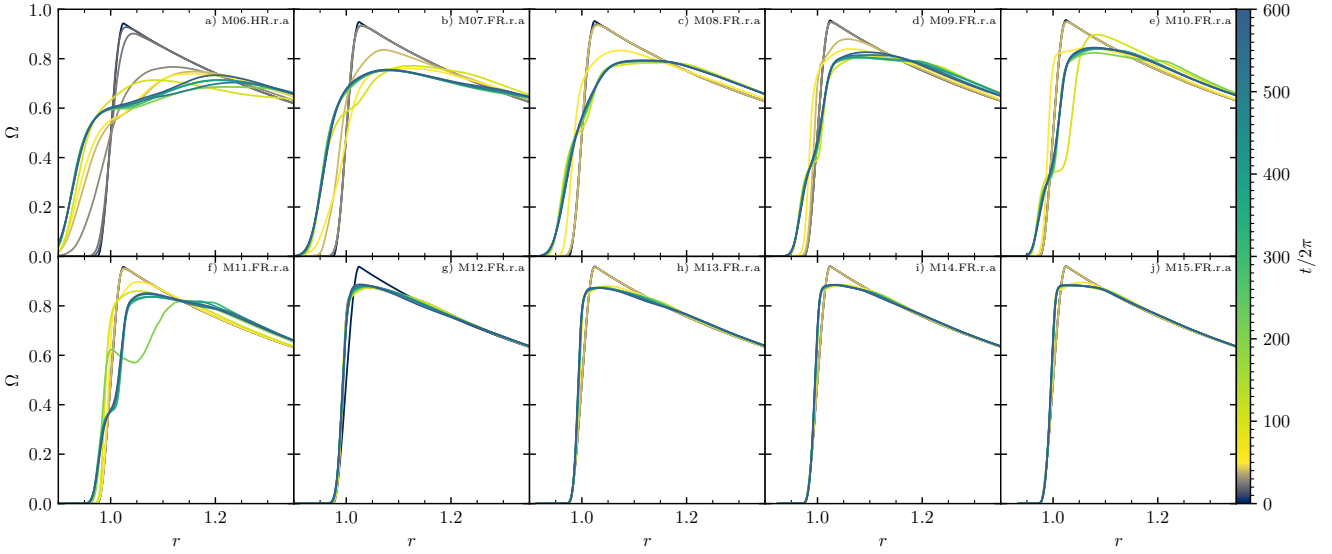


Figure 8. Evolution of $\Omega(r)$ profiles in simulations with different values of M (found in the run label). Different curves correspond to different moments of time coded in the colorbar on the right. See text for details.

erally affect disk evolution much stronger than the other types of modes. Since these modes are trapped in the resonant cavity in the inner disk, gas accretion onto the star driven by them clears out a substantial depression, or gap, in the inner disk. The development of such a gap is illustrated in the top row of Figure 4. One can see that the reduction of Σ can be quite substantial, with the gap depth reaching $\sim 80\%$ of the original density at $r \lesssim 1.5$ in simulations with $M \lesssim 9$. For higher- M runs, which often exhibit more regular patterns of the acoustic modes, the decrement of Σ is not so large, with the gap depths at the level of $\sim (20 - 30)\%$ being more typical, see Figure 4. The radial extent of the gap also decreases with increasing M , in agreement with the smaller radial width of the resonant cavity at higher M , see §5.2.

In our simulations the deepening of the gap saturates once it reaches a sufficient depth that depends on M . The gap does not get refilled by the matter arriving from larger radii, as would be expected in a real accretion disk, because our runs do not have an explicit mechanism of the angular momentum transport in the outer disk (i.e. α -viscosity or MRI). In real disks one should expect the gap to be shallower than what we find in our simulations.

8.1 Evolution of the $\Omega(r)$ profile

Sharp gradients of Σ that develop around the gap region cause substantial modification of $\Omega(r)$ profile away from the purely Keplerian $\Omega_K(r)$ in the bulk of the disk. In a steady state $\Omega(r)$ is given by

$$\Omega^2(r) = \Omega_K^2(r) + \frac{1}{\Sigma r} \frac{\partial P}{\partial r}, \quad (21)$$

following from the radial momentum balance equation. Because of the initial non-uniform profile of Σ and the resultant radial pressure gradient, some deviation of Ω from Ω_K is present even at the start of simulations.

But after the gap develops in the disk, these Ω deviations increase as the second term in the right hand side of the equation (21) becomes much larger. This is illustrated in Figure 8, which shows the profiles of $\Omega(r)$ at different moments of time in simulations with different M . Using the simulation data on $\Sigma(r)$ (e.g. the ones

shown in the top row of Figure 4) we find that the $\Omega(r)$ profile agrees very well with the equation (21). Interestingly, equation (21) describes the $\Omega(r)$ behavior quite well even inside the BL, where $\Omega(r)$ substantially deviates from Ω_K . This means that even within the BL the radial velocity of the accreting matter v_r is still quite small, so that the inertial terms in the radial momentum balance equation can be neglected.

In agreement with the equation (21), we find $\Omega < \Omega_K$ interior from the deepest part of the gap, where Σ and P decrease with radius. In fact, Ω tends to exhibit a relatively flat, *plateau-like* segment with $\Omega(r) \approx \Omega_{\max}$ just outside the BL. Right outside the deepest part of the gap, P increases with r (very strongly for lower M), driving Ω above Ω_K . This can be most easily seen in Figure 8c-f. As the gap width and depth become smaller for higher M , so does the deviation of Ω from Ω_K : the region near the BL where $\Omega(r)$ exhibits a plateau gets narrower as M grows, and the value of Ω in this region gets closer to Ω_K .

To characterize these $\Omega(r)$ features developing near the BL, in Figure 9 we plot the width of the BL δ_{BL} , defined as the radial extent over which Ω transitions from 25% to 75% of its maximum value, i.e. $\delta_{\text{BL}} \equiv R(\Omega = 0.75\Omega_{\max}) - R(\Omega = 0.25\Omega_{\max})$ (panel (a)); the deviation of $\Omega(r)$ in the plateau region $\delta\Omega$ from $\Omega_K(R_*) = 1$, i.e. $\delta\Omega \equiv 1 - \Omega_{\max}$ (panel (b)); and the radial width δ_{plateau} of the plateau in Ω , defined as the radial extent over which $\Omega \geq 0.9\Omega_{\max}$. One can see that all three plotted variables generally *decrease* with increasing M , as mentioned previously. Note that some values of M for which we have multiple simulations show a spread in these derived variables, see e.g. the variation of δ_{BL} for $M = 9$ in panel (a).

Such spreads in δ_{BL} are caused by the emergence of an inflection point in $\Omega(r)$ profile inside the BL in some runs, which acts to increase the radial range over which Ω varies. This feature is clearly seen e.g. in Figure 8d-f (see Belyaev et al. 2012 and Dittmann 2021 for similar observations). To circumvent the effect of this feature on the determination of δ_{BL} we focus on the smallest values of δ_{BL} for

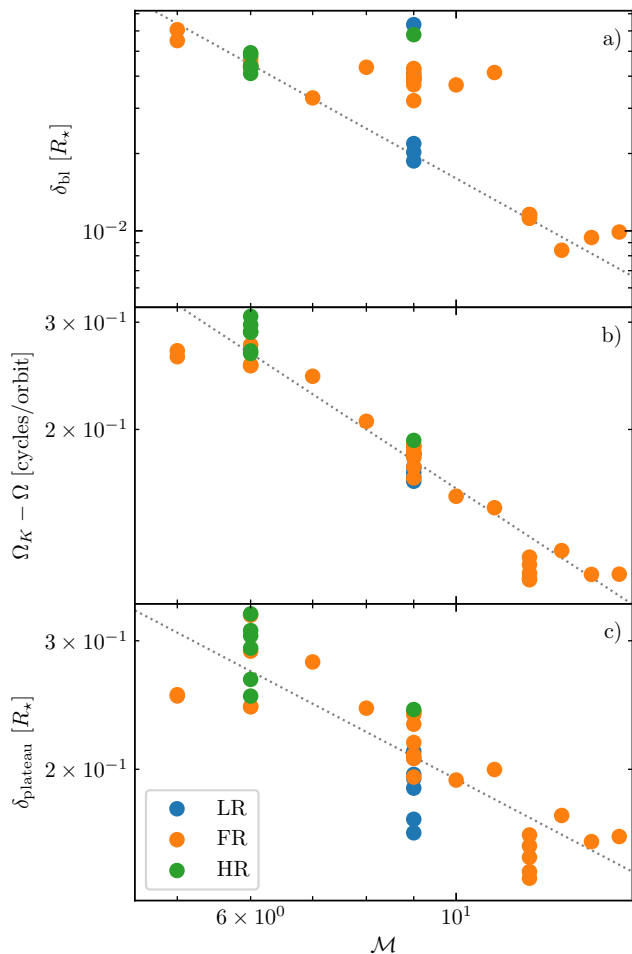


Figure 9. (a) Width of the BL as a function of \mathcal{M} ; dotted line corresponds to equation (22). (b) Deviation of the plateau from $\Omega_K(R_*)$ as a function of \mathcal{M} ; dotted line corresponds to equation (23). (c) Radial extent of the Ω plateau as a function of \mathcal{M} ; dotted line corresponds to equation (24). The dotted lines are by-eye fits to the relevant data. The data shown correspond to the final output file of each simulation ($t/2\pi = 600$).

a given \mathcal{M} . To guide the eye, in Figure 9a we run⁷ a dotted line

$$\delta_{\text{BL}} \approx 2 \mathcal{M}^{-2} \quad (22)$$

through these points that appears to provide a decent fit to the lower envelope of the measured δ_{BL} values. As previously noted in Belyaev et al. (2012), this scaling implies that δ_{BL} is equal to a fixed (i.e. independent of \mathcal{M}) number of *stellar* scaleheights (equal to \mathcal{M}^{-2} in our notation). In our case this number is ≈ 2 , which is significantly less than $7 - 8$ found in Belyaev et al. (2012), a difference naturally explained by the fact that Belyaev et al. (2012) did not attempt to account for the effect of the inflection point on the Ω profile.

In Figure 9b we plot $\delta\Omega$ — the deviation of Ω from unity in the plateau region — together with a by-eye fit

$$\delta\Omega \approx 1.5 \mathcal{M}^{-1}. \quad (23)$$

This rough scaling can be understood analytically using equation (21) if we also assume that the radial scale of Σ variation in the

gap near the stellar surface is of order of the *disk* scaleheight \mathcal{M}^{-1} , which appears to be the case in our runs. The data for the radial extent of Ω plateau δ_{plateau} is shown in Figure 9c together with a simple fit (dotted curve)

$$\delta_{\text{plateau}} \approx 0.9 \mathcal{M}^{-2/3}. \quad (24)$$

Based on the Keplerian rotation law and equation (23), one might have expected a steeper dependence on \mathcal{M} for a flat Ω plateau, closer to $\propto \mathcal{M}^{-1}$. However, examination of Figure 8 shows that approximating the $\Omega(r)$ plateau shape as flat is very approximate, and that it has a certain non-trivial radial dependence to it. Thus, the exponent in equation (24) different from -1 should not come as a surprise.

Knowledge of $\delta\Omega$ and δ_{plateau} is important since we often find the plateau region to contain near-surface vortices that drive prominent spiral arms in the disc, see Paper I. The pattern speed of such features should be roughly equal to $1 - \delta\Omega$ (as the vortices are comoving with the fluid), while δ_{plateau} informs us about the distance out to which these near-surface vortices might be expected to be found.

Given that the exact shape of the Ω plateau depends on the $\Sigma(r)$ profile in the gap, one may wonder if scalings (23), (24) would still hold in the presence of mass inflow from larger radii, which is expected in real disks. It is very likely that $\delta\Omega$ and δ_{plateau} behaviors shown in Figure 9 will change in that situation. However, the scaling (22) for the width of the BL (δ_{BL}) must be robust regardless of the presence or absence of the mass inflow, since the existence of the BL is independent of the presence or absence of a depression in Σ outside the star.

9 DISCUSSION

Results of the previous sections illustrate the important effect of the wave modes triggered by the supersonic shear inside the BL on the angular momentum and mass transport in the inner disk. We now discuss some additional aspects of the wave-driven transport processes in the vicinity of the BL.

9.1 Modes dominating mass transport and disk evolution

The discussion in §5.3.1-5.3.5 allows us to identify the modes most relevant for driving the accretion onto the star. Since accretion implies $\dot{M} > 0$, we can immediately conclude that it is the lower acoustic and resonant modes that must be responsible for driving the mass inflow onto the stellar surface. This conclusion is supported by Figure 6 and the results presented in §7, which show that the highest values of \dot{M} require $C_S < 0$, which is a unique feature of these two types of modes.

At the same time, the vortex-driven (and, at lower amplitude, the upper acoustic) modes drive a weak mass outflow in the disk, which is not conducive to accretion. In realistic disks this outflow would be suppressed by the mass inflow caused by other sources of the angular momentum transport capable of operating in the bulk of the disk, e.g. the MRI.

It is important that the \dot{M} driven by the lower acoustic and resonant modes is large only in radially narrow region of the disk near the stellar surface, where the mode is trapped. This means that these modes by themselves are not capable of maintaining constant \dot{M} through the whole disk, which would be necessary to keep it in a steady state. Other transport mechanisms are clearly needed to ensure a steady delivery of mass towards the BL, e.g. the MRI.

⁷ This and other dotted lines in Figure 9 are not formal fits to the data.

It is also important to realize that in realistic disks, inside the resonant cavity where the \dot{M} -driving modes are trapped, the angular momentum transport would be provided *both* by the waves, globally, *and* by the MRI, locally (since $d\Omega/dr < 0$ in that region, see Figure 8). This enhanced transport is likely to result in a non-trivial structure of the surface density in this near-BL part of the disk.

9.2 Global nature of the angular momentum transport

Our morphological study in Paper I demonstrates that the waves excited in the vicinity of the BL can propagate over substantial distances in the disk. This is clear for the vortex-driven and upper acoustic modes that can propagate from their corotation region near the BL all the way into the outer disk where they get gradually damped. However, even the modes which are trapped near the BL — the lower acoustic waves and the resonant modes — still travel over a significant radial range in the disk, comparable to R_\star . This is especially true for the low- m resonant modes, for which the corotation radius can lie quite far out in the disk, see Paper I.

The long-range propagation of the waves makes the angular momentum transport effected by them truly global. It gives rise to a non-local coupling between the BL, where the accreting matter uploads its angular momentum and energy to the waves, and the more distant parts of the disk, where the waves dissipate, driving \dot{M} and injecting their energy into the disk fluid (Rafikov 2016). Such non-locality is typical also for the angular momentum transport by the planet-driven density waves in the protoplanetary disks (Lunine & Stevenson 1982; Goodman & Rafikov 2001; Rafikov 2002; Rafikov & Petrovich 2012; Petrovich & Rafikov 2012).

Because of its non-locality, the wave-driven transport cannot be characterized by a single α parameter, which is often invoked to describe local transport (Shakura & Sunyaev 1973; Balbus & Papaloizou 1999). As we demonstrate in §5.4, the values of α near the BL computed using stress C_S and \dot{M} (which are the same for local transport) are different not only in magnitude but also in sign, see Figure 4. For that reason, the standard methods for calculating the structure and viscous evolution of the disk based on the diffusion-type equation approach (Lynden-Bell & Pringle 1974), would fail to describe the disk in the vicinity of the BL. Instead, calculations of the wave-mediated structure of the inner disk need to explicitly account for the long-range propagation and dissipation of the waves excited in the BL.

9.3 Observational implications

Non-local wave-driven transport effected by the waves has important implications for the observational appearance of the objects accreting through the BL. Models of the BL structure using the local α -viscosity inevitably predict that local energy dissipation in the layer should heat gas in the BL to high temperatures (Popham et al. 1993; Narayan & Popham 1993). This would naturally give rise to a high-energy component in the spectra of objects accreting through the BL, which is often not observed (Ferland et al. 1982).

Energy transport by the waves changes the whole pattern of the energy dissipation: it occurs not in the narrow BL itself, but over a larger area of the disk, lowering the effective temperature of emission associated with the BL and naturally alleviating the "missing boundary layer" problem (Ferland et al. 1982). The rate $d\dot{E}/dr$ (per unit time and radius) at which thermal energy is deposited in the disk by a wave (with pattern speed Ω_P) is closely

related to the rate of dissipation of the wave angular momentum flux, as $d\dot{E}/dr = (\Omega - \Omega_P)dC_S/dr$ (Lynden-Bell & Kalnajs 1972; Goodman & Rafikov 2001; Rafikov 2016). Thus, the results of our study on the radial profiles of C_S for different wave modes can be directly employed to analyze the spatial distribution of the disk heating induced by the BL-excited waves.

9.4 Comparison with the existing studies

In the past, Belyaev et al. (2012, 2013a,b) analyzed the behavior of the wave angular momentum flux C_S in the vicinity of the BL, and related it to the \dot{M} behavior and the wave amplitude in the disk. More recently, Dittmann (2021) looked at the C_S behavior in the disk (as well as the flow of mass and angular momentum into the star) for non-zero stellar spin rates. Our present work goes beyond these studies in several ways.

First, we analyze C_S behavior for a variety of *individual* modes present in the disk. Coupling this with the results of our morphological study in Paper I allows us to understand the C_S behavior for each mode type — lower and upper, resonant, vortex-driven, and so on. Second, we follow how the behavior of C_S changes as our simulations progress and different types of wave modes come and go. Third, we systematically explore the differences in the C_S behavior as a function of the Mach number \mathcal{M} of our runs.

10 SUMMARY

In this work we studied the angular momentum and mass transport driven by the different types of the waves operating in the vicinity of the BL of an accretion disk. Our analysis is based on a large suite of global, 2D hydrodynamic simulations described in Paper I, in which a large number of modes have been previously identified and characterized. Results of our present study can be summarized as follows.

- In wave-mediated inner region of the disk mass accretion rate \dot{M} has a significant contribution arising from the correlated radial velocity v_r and the surface density perturbation $\delta\Sigma$.
- The efficiency of angular momentum transport expressed through the effective α -parameter appears to not depend strongly on the Mach number of the flow \mathcal{M} .
- By examining angular momentum flux $C_{S,m}$ carried by each individual Fourier harmonics, we were able to determine the transport properties associated with each type of the mode for different values of the Mach number \mathcal{M} . In particular, we find that lower acoustic and resonant modes carry negative angular momentum flux, whereas the vortex-driven and upper acoustic modes carry positive angular momentum flux.
- Nonlinear damping of the modes leads to mass inflow ($\dot{M} > 0$) for the lower acoustic and resonant modes, and weak mass outflow for the vortex-driven and upper acoustic modes. This implies that accretion onto the central object must be mediated by a combination of the lower acoustic and resonant modes.
- Wave-driven transport is intrinsically non-local, which leads to the values of effective α -parameter determined through stress and \dot{M} being different not only in amplitude but also in sign. This is very different from the conventional local transport for which these values are the same.
- Despite the non-local nature of the wave-mediated transport we still find a strong correlation, given by the equation (20), between the angular momentum flux injected at the BL into the disk, and the mass accretion rate through the BL.

- Despite the long duration of our simulations, we find the time-dependent contribution to the angular momentum balance caused by the variation of Ω (see equation (9)) to play an important role (see §6).

- We characterize the wave-driven evolution of the disk properties — surface density Σ and angular frequency Ω profile — as a function of time and M .

Our study, based on 2D hydro simulations, provides a natural foundation for understanding the properties of the wave-driven transport in future three-dimensional and fully MHD simulations of the BLs.

ACKNOWLEDGEMENTS

We thank Jim Stone for making the Athena++ code publicly available. We gratefully acknowledge financial support from NSF via grant AST-1515763, NASA via grant 14-ATP14-0059, and Institute for Advanced Study via the John N. Bahcall Fellowship to R.R.R. Research at the Flatiron Institute is supported by the Simons Foundation. Resources supporting this work were provided by the NASA High-End Computing (HEC) Program through the NASA Advanced Supercomputing (NAS) Division at Ames Research Center. Through allocation AST160008, this work used the Extreme Science and Engineering Discovery Environment (XSEDE), which is supported by National Science Foundation grant number ACI-1548562 (Towns et al. 2014).

DATA AVAILABILITY

The data underlying this article will be shared on reasonable request to the corresponding author.

REFERENCES

- Arzamasskiy L., Rafikov R. R., 2018, *The Astrophysical Journal*, 854, 84
 Balbus S. A., Hawley J. F., 1991, *ApJ*, 376, 214
 Balbus S. A., Hawley J. F., 1998, *Reviews of Modern Physics*, 70, 1
 Balbus S. A., Papaloizou J. C. B., 1999, *ApJ*, 521, 650
 Balsara D. S., Fisker J. L., Godon P., Sion E. M., 2009, *ApJ*, 702, 1536
 Belyaev M. A., Quataert E., 2018, *MNRAS*, 479, 1528
 Belyaev M. A., Rafikov R. R., 2012, *ApJ*, 752, 115
 Belyaev M. A., Rafikov R. R., Stone J. M., 2012, *ApJ*, 760, 22 (BRS)
 Belyaev M. A., Rafikov R. R., Stone J. M., 2013a, *ApJ*, 770, 67 (BRS1)
 Belyaev M. A., Rafikov R. R., Stone J. M., 2013b, *ApJ*, 770, 68 (BRS2)
 Coleman M. S. B., Rafikov R. R., Philippov A. A., 2021, *MNRAS*,
 Dittmann A. J., 2021, *MNRAS*, 508, 1842
 Ferland G. J., Langer S. H., MacDonald J., Pepper G. H., Shaviv G., Truran J. W., 1982, *ApJ*, 262, L53
 Flock M., Dzyurkevich N., Klahr H., Turner N. J., Henning T., 2011, *ApJ*, 735, 122
 Fromang S., Nelson R. P., 2006, *A&A*, 457, 343
 Ghosh P., Lamb F. K., 1978, *ApJ*, 223, L83
 Gnedin O. Y., Goodman J., Frei Z., 1995, *AJ*, 110, 1105
 Goodman J., Rafikov R. R., 2001, *ApJ*, 552, 793
 Hertfelder M., Kley W., 2017, *A&A*, 605, A24
 Ju W., Stone J. M., Zhu Z., 2016, *ApJ*, 823, 81
 Koenigl A., 1991, *ApJ*, 370, L39
 Landau L. D., Lifshitz E. M., 1959, *Fluid mechanics*. Pergamon Press
 Larson R. B., 1984, *MNRAS*, 206, 197
 Larson R. B., 1990, *MNRAS*, 243, 588
 Lunine J. I., Stevenson D. J., 1982, *Icarus*, 52, 14
 Lynden-Bell D., Kalnajs A. J., 1972, *MNRAS*, 157, 1

- Lynden-Bell D., Pringle J. E., 1974, *MNRAS*, 168, 603
 Narayan R., Popham R., 1993, *Nature*, 362, 820
 Pessah M. E., Chan C.-k., 2012, *ApJ*, 751, 48
 Petrovich C., Rafikov R. R., 2012, *ApJ*, 758, 33
 Popham R., Narayan R., Hartmann L., Kenyon S., 1993, *ApJ*, 415, L127
 Rafikov R. R., 2002, *ApJ*, 569, 997
 Rafikov R. R., 2016, *ApJ*, 831, 122
 Rafikov R. R., Petrovich C., 2012, *ApJ*, 747, 24
 Shakura N. I., Sunyaev R. A., 1973, *A&A*, 24, 337
 Spruit H. C., 1987, *A&A*, 184, 173
 Stone J. M., Tomida K., White C. J., Felker K. G., 2020, *ApJS*, 249, 4
 Towns J., et al., 2014, *Computing in Science & Engineering*, 16, 62
 Velikhov E. P., 1959, *Journal of Experimental and Theoretical Physics*, 36, 995

APPENDIX A: DETAILS OF THE TIME-AVERAGING PROCEDURES

Here we summarize the technical details of various averaging and smoothing procedures that were used in analyzing the data and producing various plots. For all the line plots in this paper (except for Fig. 8) we used the unbinned FFT data to measure azimuthal averages ($m = 0$; all the quantities inside angular brackets) and higher order $m > 0$ modes with high cadence (exactly 20 outputs per orbit with non uniform cadence; see Paper I for more details). As the final step of the calculation we average in time over the intervals denoted in the figures. For Figs. 2 and 3 we chose to plot only the five modes with the largest time (over the interval noted in the figure) and radially (over $r > 1$) integrated $|C_{s,m}|$.

We examine Eqn. (9) in Fig. 5. We rewrite and expand this equation below to be explicit about the averaging done in the figure:

$$\underbrace{2\pi r \langle \Sigma v_r \rangle}_{M \partial_r \ell} \frac{\partial}{\partial r} \left(r \frac{\langle \Sigma v_\phi \rangle}{\langle \Sigma \rangle} \right) = \underbrace{\frac{\partial C_S}{\partial r}}_{\partial_r C_S} + \underbrace{2\pi r^2 \langle \Sigma \rangle \frac{\partial}{\partial t} \frac{\langle \Sigma v_\phi \rangle}{\langle \Sigma \rangle}}_{\text{“}\partial_t v_\phi\text{”}}$$

where C_S is computed using Eqns. (6) and (8), and the underbraces are used to denote how the terms are labeled in Fig. 5. All the azimuthally averaged quantities (i.e. the ones in angular brackets) are measure directly from the $m = 0$ mode of our high cadence FFT data as explained above. The partial derivative with respect to time is computed via finite differences on the high cadence FFT data to second order accuracy. After these computations are completed the data is averaged in time over the time interval shown in the figure.

This paper has been typeset from a $\text{\TeX}/\text{\LaTeX}$ file prepared by the author.